1-1-2014

A comprehensive computational model of sound transmission through the porcine lung

Zoujun Dai

Ying Peng

Brian M. Henry

Hansen A. Mansy
University of Central Florida

Richard H. Sandler

See next page for additional authors

Authors

Zoujun Dai, Ying Peng, Brian M. Henry, Hansen A. Mansy, Richard H. Sandler, and Thomas J. Royston

A comprehensive computational model of sound transmission through the porcine lung

Zoujun Dai, Ying Peng, Brian M. Henry, Hansen A. Mansy, Richard H. Sandler, and Thomas J. Royston

---

ARTICLES YOU MAY BE INTERESTED IN

Boundary element model for simulating sound propagation and source localization within the lungs
The Journal of the Acoustical Society of America **122**, 657 (2007); https://doi.org/10.1121/1.2715453

A multiscale analytical model of bronchial airway acoustics
The Journal of the Acoustical Society of America **142**, 1774 (2017); https://doi.org/10.1121/1.5005497

Modeling sound transmission through the pulmonary system and chest with application to diagnosis of a collapsed lung
The Journal of the Acoustical Society of America **111**, 1931 (2002); https://doi.org/10.1121/1.1452742

Localization of adventitious respiratory sounds
The Journal of the Acoustical Society of America **143**, 1297 (2018); https://doi.org/10.1121/1.5025842

Sound propagation through human lungs, under transmission sounding with acoustic signal of 80-1000 Hz frequency band
Proceedings of Meetings on Acoustics **23**, 020002 (2015); https://doi.org/10.1121/2.0000077

A comprehensive computational model of sound transmission through the porcine lung
The Journal of the Acoustical Society of America **134**, 4121 (2013); https://doi.org/10.1121/1.4831141

A comprehensive computational model of sound transmission through the porcine lung

Zoujun Dai[a)]
Department of Bioengineering, University of Illinois at Chicago, Chicago, Illinois 60607

Ying Peng
Department of Mechanical and Industrial Engineering, University of Illinois at Chicago, Chicago, Illinois 60607

Brian M. Henry
Department of Bioengineering, University of Illinois at Chicago, Chicago, Illinois 60607

Hansen A. Mansy
Department of Mechanical and Aerospace Engineering, University of Central Florida, Orlando, Florida 32816

Richard H. Sandler
Nemours Children Hospital, Orlando, Florida 32827

Thomas J. Royston
Department of Bioengineering, University of Illinois at Chicago, Chicago, Illinois 60607

A comprehensive computational simulation model of sound transmission through the porcine lung is introduced and experimentally evaluated. This "subject-specific" model utilizes parenchymal and major airway geometry derived from x-ray CT images. The lung parenchyma is modeled as a poro-viscoelastic material using Biot theory. A finite element (FE) mesh of the lung that includes airway detail is created and used in COMSOL FE software to simulate the vibroacoustic response of the lung to sound input at the trachea. The FE simulation model is validated by comparing simulation results to experimental measurements using scanning laser Doppler vibrometry on the surface of an excised, preserved lung. The FE model can also be used to calculate and visualize vibroacoustic pressure and motion inside the lung and its airways caused by the acoustic input. The effect of diffuse lung fibrosis and of a local tumor on the lung acoustic response is simulated and visualized using the FE model. In the future, this type of visualization can be compared and matched with experimentally obtained elastographic images to better quantify regional lung material properties to noninvasively diagnose and stage disease and response to treatment. © 2014 Acoustical Society of America. [http://dx.doi.org/10.1121/1.4890647]

I. INTRODUCTION

A. Motivation

The lungs are a unique, multiphase porous structure that have defied conventional noninvasive medical imaging methods and our ability to contrast and quantify changes in macroscopic properties that can be indicative of disease and be fundamentally linked to pathophysiologic and structural changes at the microscopic level. A wide range of pulmonary ailments can result in significant changes, locally or diffusely, to the stiffness or density of lung tissue with findings that include inflammation, fibrosis, edema, consolidation, or a mass effect (e.g., tumors). These changes often are not easily identifiable by currently available imaging modalities.

The utility of conventional ultrasound pulmonary imaging is limited due to the acoustic impedance mismatch between the air in the lungs and soft tissue. X-ray computed tomography (CT) and magnetic resonance imaging (MRI) provide useful anatomic information but are often limited in their diagnostic accuracy, especially in distinguishing benign, infectious, and malignant pathologies. CT also has the disadvantage of cancer risk associated with ionizing radiation. MRI using RF tagging has been suggested as a method for assessing the regional mechanical properties of the parenchyma;[1,2] but this approach has been limited to assessing changes in lung volume throughout the respiratory cycle.

Alterations in the structure and function of the pulmonary system that occur in disease or injury often give rise to measurable changes, spatially and temporally, in lung sound production and transmission that, if properly quantified, might provide additional information about the etiology, severity, and location of trauma injury or other pathology.[3–6] Indeed simultaneous, multi-sensor auscultation methods have been developed to "map" sounds on the thoracic surface by several groups.[5,7–11] Also recently the phase contrast-based technique known as magnetic resonance

a)Author to whom correspondence should be addressed. Electronic mail: zdai3@uic.edu

elastography (MRE) has been applied to the lungs in pilot studies with limited success.[12–15] MRE seeks to provide a map of the viscoelastic properties within the region of interest that will affect the shear wave motion that MRE measures. Previously MRE has been successfully applied to the study of the mechanical properties of a variety of other organs and soft tissue regions *in vivo*, including the breast, brain, kidney, prostate, liver, and muscle.[16–20] Application to the lungs has proven more challenging given the poor signal-to-noise available in imaging due to a lower presence of hydrogen in air than in soft tissue (containing water) and the complex nature of vibratory wave propagation found in the lungs. A better understanding of mechanical wave motion in the lungs would aid in the interpretation of the wave images that are acquired using MRE to reconstruct a quantitative map of variation in mechanical properties that can correlate with injury, the progression of disease, and/or the response to therapy.

B. Literature review

The lung parenchyma is comprised of soft biological tissue and vasculature as well as millions of microscopic air sacs (alveoli) that are connected through a complex branching airway structure. Microscopically the lungs are highly heterogeneous in terms of their physical properties, combining gas (air) that is linked through a complex and tortuous network of channels and microscopic sacs, non-Newtonian liquid (blood) that flows through an equally complex network of vessels of wide-ranging dimensions, and viscoelastic soft tissue structures that exhibit nonlinear behavior under large deformation.

Sound transmission in the pulmonary system can be analyzed by separating it into the airway acoustics and lung parenchymal acoustics. The acoustics of the respiratory airway tract can be further separated into the supraglottal and subglottal components. Our focus here is the subglottal region, which consists of the trachea that splits into the main-stem bronchi, which further divide numerous times to create the complex bronchial trees. While the bronchial tree is extremely complex, geometrically it will exhibit less temporal variability as voluntary actions of the subject will not significantly alter its geometry This is unlike the supraglottal region where subject ability can alter the glottal opening, tongue position, throat, and mouth geometry, etc. In this article, a comprehensive technique for relating the acoustic pressure throughout the bronchial tree to the acoustic pressure just below the glottis is developed.

The model of sound propagation in the subglottal airways consists of two fundamental parts. First, it requires a mathematical description of the acoustic properties of individual airway segments, the description of which must be sufficiently sophisticated to include all significant acoustic phenomena of the gas and airway walls. Second, the dynamic description of individual airway segments must be integrated into a complex asymmetric airway tree encompassing up to several million branch segments if one attempts to model airway details down to the aveoli. This task can be tackled by using the Horsfield self-consistent model of asymmetric dichotomy for the bronchial tree.

Horsfield *et al.*[21,22] proposed an approximate but comprehensive model based on detailed lung castings for both human and canine subjects. The Horsfield model of the human lung categorizes the airway tree into 35 different segment sizes, starting with $n = 35$, the trachea, and ending with $n = 1$, the terminal bronchiole, which itself terminates into two alveoli. It specifies the degree of asymmetry at each airway bifurcation through a recursion index called $\Delta^{(n)}$. An airway of order n bifurcates into two airways of order $n–1$ and $n–1-\Delta^{(n)}$. The Horsfield model is self-consistent in the sense that, for a particular airway order n, the bifurcated airway types (or daughter airways) are the same throughout the lung. A partial diagram of the lung airway tree based on this model down to $n = 11$ can be found in Fredburg *et al.*[23]

For the purpose of developing a tractable set of equations for predicting small-amplitude mechanical wave motion in the parenchyma for wavelengths larger than the microscopic heterogeneous features of the lung, macroscopic homogenized representations of the lung's physical properties have been proposed.[24–28] Based on this homogenous or stochastic spatially averaged view, two different models for wave propagation have been put forth. One is sometimes referred to as the "effective medium" or "bubble swarm" theory. It has been prominently used in the literature for modeling lung acoustics since the 1980s.[24–26] More recently, there has been an interest in applying Biot's theory of poroelasticity to the lung parychyma.[27,28] Application of Biot theory leads to a more complex theoretical model that predicts more wave types as compared to the effective medium theory.

C. Objectives of this study

The objective of the present study is to introduce and experimentally validate a comprehensive computational simulation model of sound transmission through the porcine lung. Airway and lung parenchymal acoustics are reviewed in Sec. II. Experimental measurements on the surface of the excised lung using scanning laser Doppler vibrometry are covered in Sec. III. The subject-specific model utilizing parenchymal and major airway geometry derived from x ray CT images is described in Sec. IV. The lung parenchyma is modeled as a poroviscoelastic material using Biot theory. A finite element (FE) mesh of the lung that includes airway details is created and used in COMSOL FE software to simulate the vibroacoustic response of the lung due to sound input at the trachea. In Sec. V, the FE simulation model is validated by comparing simulation results to experimental measurements on the surface of the excised lung acquired using scanning laser Doppler vibrometry. The FE model is also used to calculate and visualize vibroacoustic pressure and motion inside the lung and its airways caused by the acoustic input. Finally the effect of diffuse lung fibrosis and a local tumor on the lung acoustic response is simulated and visualized using the FE model.

II. THEORY

A. Airway acoustics

It is of interest in the present study to be able to calculate the acoustic impedance (ratio of acoustic pressure to

Dai *et al.*: Computational lung sound transmission model

acoustic particle velocity as a function of frequency) as a function of the airway geometry and frequency. The Horsfield model, as modified by Habib et al.[29,30] to account for non-rigid airway walls and terminal respiratory tissues renders this task possible. The first step is to calculate the input acoustic impedance at a terminal bronchiole, $n = 1$. Then "march up" the recursion ladder from $n = 2$, then 3 and so on until calculating the input impedance for $n = 35$, the trachea. Referring to Fig. 1, for the nth order airway segment of length $l^{(n)}$, the input acoustic impedance $Z_{in}^{(n)}[\omega]$ (taken at the end closer to the trachea) is given by

$$Z_{in}^{(n)}[\omega] = \frac{Z_T^n[\omega] + Z_0^n[\omega]\tanh\left[\gamma_0^{(n)}[\omega]l^{(n)}\right]}{1 + \left(Z_T^n[\omega]/Z_0^n[\omega]\right)\tanh\left[\gamma_0^{(n)}[\omega]l^{(n)}\right]},$$
$$n = 1, \ldots, 35. \quad (1)$$

The terms $Z_0^{(n)}[\omega]$ and $\gamma_0^{(n)}[\omega]$ are the characteristic impedance and propagation coefficient of the nth airway segment, respectively, and are given in Royston et al.[31]

The term $Z_T^{(n)}[\omega]$ denotes the acoustic impedance at the far end of each segment, which is given by

$$Z_T^{(n)}[\omega] = \begin{cases} \dfrac{N_T}{j\omega C_g + 1/[R_t + j(\omega I_t - 1/[\omega C_t])]}, \\ \quad n = 1 \\ \dfrac{1}{1/Z_{in}^{(n-1)}[\omega] + 1/Z_{in}^{(n-1-\Delta[n])}[\omega]}, \\ \quad n = 2, \ldots, 35. \end{cases} \quad (2)$$

Here N_T denotes the total number of terminal ($n = 1$) bronchiole segments, which are effectively in parallel with respect to the termination into the soft tissue of the parenchyma. For the Horsfield model, this can be calculated using the following recursion formula, taking $Z_T^{(1)} = 1$ and $N_T = Z_T^{(35)}$,

$$N_T^{(n)} = N_T^{(n-1)} + N_T^{(n-1-\Delta[n])}. \quad (3)$$

The result is $N_T \approx 2.35 \times 10^6$ in this case. The term C_g denotes the alveolar gas compression compliance based on the Dubois six-element terminal airway model.[32] Also based on the Dubois model, R_t, I_t, and C_t denote the terminal tissue resistance, inertia, and compliance, respectively.
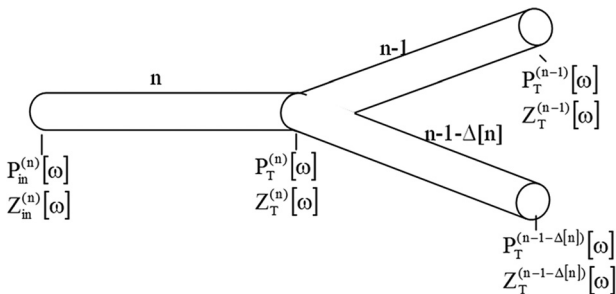

FIG. 1. Airway acoustic model showing one bifurcation.

1. Parenchymal acoustics

In previous studies by the authors, Biot theory of wave propagation in poroviscoelastic media and the effective medium theory were used to model sound transmission in the lung parenchyma.[28] Measurements of compression wave speed and attenuation in freshly exercised pig lung matched theoretical predictions based on Biot theory much more closely than did the effective medium theory. The shear wave propagation in the lung was also well predicted by the Biot theory. As presented in Schanz,[33] the following set of coupled differential equations (written in the Laplace domain where multiplication by s denotes a derivative with respect to time) describes dynamic oscillatory displacement u of the lung parenchyma and dynamic pressure p of the air in the lung,

$$\mu u_{i,jj} + \left(K_b + \frac{\mu}{3}\right)u_{j,ij} - (\alpha - \beta)p_{,i} = s^2\left(\rho - \beta\rho_f\right)u_i, \quad (4a)$$

$$\beta p_{,ii} - \frac{\phi^2}{R}\rho_f s^2 p = \rho_f s^2 (\alpha - \beta)u_{i,i}. \quad (4b)$$

Here μ is the lung parenchyma shear modulus, K_b is the lung parenchyma bulk modulus. ρ is the lung density, ρ_f is the air density, ϕ is the air volume fraction in the lung, α, β, and R are the coupling parameters between the lung parenchyma and the air. Based on Eq. (4), the shear wave speed is given by

$$c_s = \sqrt{\mu/(\rho - \beta\rho_f)} \cong \sqrt{\mu/\rho}. \quad (5)$$

The coupled Eq. (4) leads to two compression waves, a fast wave and a slow wave with much larger attenuation. The compression wave speeds are given by

$$c_{pf} = \omega/k_{pf}, \quad (6a)$$

$$c_{ps} = \omega/k_{ps}. \quad (6b)$$

Here c_{pf} and c_{ps} are the fast and slow compression wave speeds, respectively. Their corresponding wave numbers, k_{pf} and k_{ps}, are derived from Eq. (4). In our frequency range of interest (100–2000 Hz), the slow compression wave cannot propagate as the relative motion between the lung parenchyma and air is impeded by viscous drag.[28] Hence only the fast compression wave can propagate in the parenchyma.

As the lung parenchyma is viscoelastic, the shear wave speed is frequency-dependent. From Eq. (5) the phase speed and attenuation are expressed in the complex valued shear wave speed. The compression wave attenuation is mainly due to the friction between the air and the lung parenchyma. The complex-valued fast compression wave speed is given by Eq. (6a).

III. EXPERIMENT

SLDV measurements (Polytec PSV-400) on the surface of one suspended excised, preserved porcine lung (ENasco,

Fort Atkinson, WI) subject to airway insonification were taken as shown in Fig. 2. The preserved lung was hung under a frame and inflated to a pressure of 20 cm H_2O transpulmonary pressure for 1 h before the experiment to help open the airways. During the experiment, that pressure was kept constant. Broad band sound (periodic chirp with spectral content from 50 to 1000 Hz and amplitude of about 1 Pa) generated by a 3.5 in. speaker (PDWR30W, PylePro, Brooklyn, NY) was sent into the excised lung via the trachea. P-RETRO-250 glass beads (45–63 μm diameter, Polytec, Irvine, CA) were spread on and adhered to the lung surface to enhance the laser reflectivity. The whole lung was scanned by the SLDV except the areas where the left and right lobe touched each other and some peripheral points without a clear line of sight to the laser. Four scans were made at different angles and then combined to cover the entire lung geometry. As the sound wave sent into the trachea is frequency-dependent, a PCB 1/4 in. microphone (377A01, PCB Piezotronic, Depew, NY) was inserted into the trachea 5 cm below the trachea opening to measure the sound pressure as a reference signal. The lung was preserved using propylene glycol, and its mechanical properties were stable and, although not the same, appeared close to that of live or freshly excised lung. The stability of the preserved lung enabled repeated measurements on the lung that take time. The SLDV measurements will be compared with computer simulations of lung excitation caused by airway insonification in Sec. V.

IV. SIMULATION

A. Lung and airway geometry construction

The preserved pig lung used in Sec. III was inflated at 20 cm H_2O transpulmonary pressure and scanned in a CT scanner (Brilliance 64, Philips Electronics) with in plane pixel resolution of 512×512 and axial steps of 1 mm. The lung contour was constructed by importing the CT images into MIMICS 14 (Materialise Group, Leuven, Belgium).

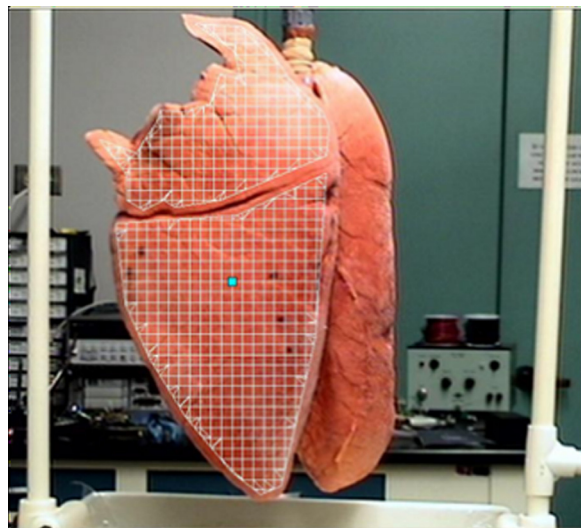The geometry of pig lung airways was generated using an open source code medical image segmentation software ITK-SNAP Version 2.4 CT images were imported for automatic segmentation using the snake algorithm in ITK-SNAP. The implementation of automatic segmentation allowed for a virtual base geometry to be constructed that was used as a baseline for later models. Because of the way that automatic segmentation works in ITK-SNAP, however, only about 20 airway segments were created because the quality of the segmentation is directly proportional to the quality of the image. The airway tree generated by automatic segmentation is called airway network 1. The white contrast was used for the automatic segmentation algorithm. The small airway segments were generated manually as their CT image resolution is beyond the automatic segmentation algorithm. This was done by marking the airway segments with the marker tool in contrasted regions slice by slice. This procedure helped construct a more complex and intricate airway tree (airways with a diameter of <3 mm, the limit of the CT imaging, where the final model had around 500 segments). That model was called airway network 2. The lung CT images used for segmentation are shown in Fig. 3. The black regions inside the lung contour are the lung parenchyma, the white regions are the airway wall, and the marked regions enclosed by the white regions are the air inside the airway. The images of Figs. 3(a) and 3(b) are identical except for the difference in the labeled airways. Figure 3(a) shows the CT image with the labeling region for airway network 1, and Fig. 3(b) shows the labeling region for airway network 2.

When the automatic and manual segmentation was completed for the airways, an additional manual segmentation step was performed on a thickness region surrounding the trachea and main stem bronchi. When all of the segmentation was completed, a surface tessellation algorithm was applied by ITK-SNAP to capture the three dimensional geometrical data, and these geometrical data were exported as a stereolithography (STL) CAD file so that they could be meshed properly in ANSYS. Figure 4 shows the geometry of the two constructed airways.

B. FE simulation of sound transmission in the lung

Once the airway and thickness geometries were imported to ANSYS ICEM CFD 12.1 (Ansys Inc., Canonsburg, PA), a meshing tool provided by ANSYS, they

FIG. 2. (Color online) Experimental setup of SLDV measurement of lung surface motion.
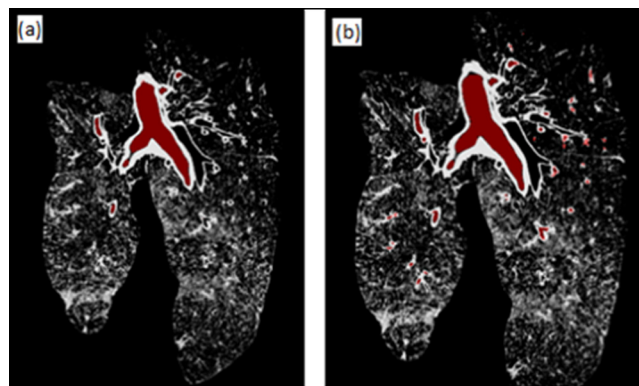

FIG. 3. (Color online) Lung CT images used for segmentation: (a) Airway network 1, (b) airway network 2.
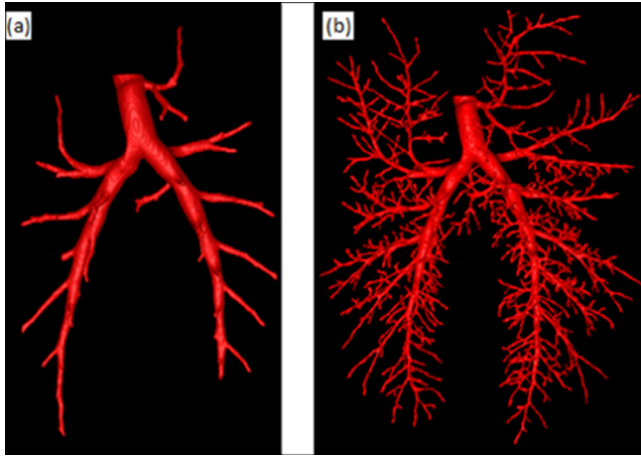
FIG. 4. (Color online) Geometry of the constructed airways: (a) Airway network 1, (b) airway network 2.

FIG. 6. (Color online) (a) Selected points on lung geometry for surface velocity amplitude comparison with experiment, (b) airway network 2 with terminal impedance specified.

were combined with the geometry of the lung parenchyma. After the geometry was checked in ANSYS for mesh quality, it was volume meshed to create a FE model. The volume mesh was imported into COMSOL 4.3a (Comsol Inc., Burlington, MA) for simulation. Figure 5 shows the volume mesh of the preserved pig lung with the different airway trees. In Fig. 6(a), four points on each side of the lung were selected, and the surface velocity amplitude at these points will be compared with corresponding locations in the preserved lung in Sec V. The airway tree lumen was specified as air in COMSOL. The airway wall was a thin layer of about 2–3 mm surrounding the lumen, and the rest of the mesh is the lung parenchyma. At the air-airway wall interface, there is continuity of normal velocity and pressure as the air is assumed to be inviscid in the simulation. At the airway wall-lung parenchyma interface, there is continuity of displacement and normal stress. The acoustic structure interaction module of COMSOL 4.3a was used to simulate sound transmission in the preserved lung. The lung parenchyma was modeled as a viscoelastic solid by specifying its complex compression and shear wave speed. The airway wall was modeled as a viscoelastic solid by specifying its complex Young's modulus taken from Suki et al.[34] Both airway networks 1 and 2 are simplified airway trees; their distal airway segments are un-
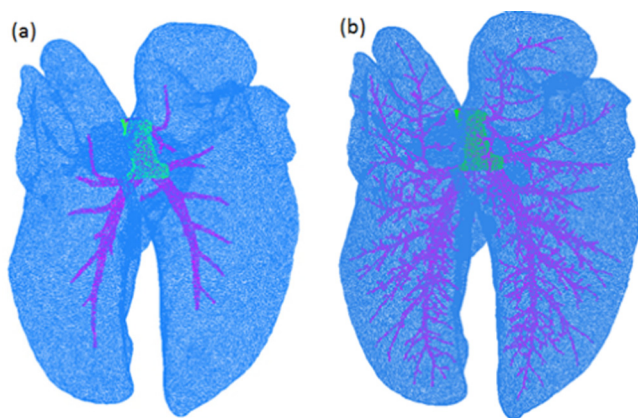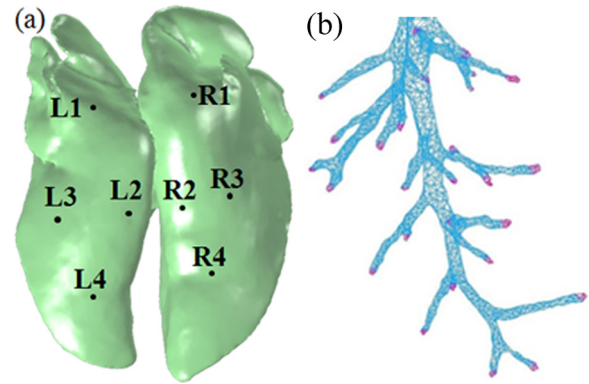
modeled due to the limit of the CT image resolution. So the terminal impedance of the terminal segments (segment which stops bifurcating into daughter segments) needs to be calculated to represent the un-modeled downstream airways. The observed morphometry of the pig airway tree appeared to be close to that of the human airway tree, especially the segments with small diameters. The Horsfield model is a structural model that is used for most mammalian airway trees; to the best knowledge of the authors, there is no such detailed structural parameters (including the order number and recursion index) for the pig airway tree. So the human airway structural parameters are used to calculate the pig airway terminal impedance. An order number needs to be specified for the terminal segments of pig airway networks 1 and 2. The standard deviation of the terminal segment diameter is small such that the terminal segments are regarded as the same, and their order number is found by relating their mean diameter to the closest value in Table 9-2 in Royston et al.[31] For airway networks 1 and 2, their terminal segment mean diameter is 0.258 and 0.115 cm, respectively; these correspond to the order numbers 17 and 12, respectively. Then the terminal impedance can be calculated by Eq. (2). Figure 6(b) shows some terminal segments of airway network 2 where the terminal impedances were specified. A harmonic sound pressure input of amplitude 1 Pa was applied at the trachea inlet. The number of tetrahedral elements of the lung with airway network 1 and airway network 2 is 748 583 and 842 607, respectively. To ensure convergence and accuracy, the element size was kept smaller than the one-sixth of compression wave length at 800 Hz. The simulation was performed from 225 to 800 Hz (as opposed to 50–1000 Hz in the experiment as the signal to noise ratio in the experiment was poor below 225 Hz and above 800 Hz) with an increment of 25 Hz. The lung density at 20 cm H_2O is taken to be 250 kg/m^3. The airway wall tissue density is taken to be 1000 kg/m^3 and its Poisson's ratio to be 0.49998. The compression speed c_p and shear wave speed c_s, the terminal impedance of airway networks 1 and 2 ($Z_T^{(17)}$ and $Z_T^{(12)}$), and the airway Young's modulus E are all frequency-dependent and they are listed in Table I for 500 and 800 Hz. The lung shear modulus was measured by the surface wave method[35] and fit by a fractional Voigt model as

FIG. 5. (Color online) Volume mesh of lung with airway tree: (a) With airway network 1, (b) with airway network 2.

J. Acoust. Soc. Am., Vol. 136, No. 3, September 2014

Dai et al.: Computational lung sound transmission model   1423

$\mu = [3.67 \times 10^3 + 235.09(j\omega)^{0.43}]$ Pa. The complex shear wave speed was derived from Eq. (5) The compression wave speed was calculated by Eq. (6a).

C. Effects of diffuse lung fibrosis and local tumor

Many pulmonary ailments such as inflammation, fibrosis, edema, and tumors result in significant changes, locally or diffusely, to the stiffness or density in the lungs that will affect wave propagation in the lungs. The FE simulation enables the visualization of the wave field in the lungs and can provide insight into changes in stiffness or density. Lung fibrosis and tumors are simulated as two representative pulmonary pathologies. It is reported that bleomycin-induced lung fibrosis locally increases median tissue stiffness two to six times relative to normal lung parenchyma.[36,37] To the best knowledge of the authors, there are no reports in literature about the macroscopic shear viscosity of fibrotic lung tissue under our frequency range of interest (100–2000 Hz). The macroscopic shear viscoelastic properties of lung tumors are also lacking in the literature. Sinkus et al.[16] applied harmonic shear wave excitation at 65 Hz and a direct-inversion modulus estimation to compare in vivo measurements made in six human breast-fibroadenoma patients with the results from six breast-carcinoma patients. Both the shear stiffness and shear viscosity of fibroadenomas and carcinomas were larger than the surrounding normal tissue. The shear viscosity had a large variation while it was easier to differentiate malignancy from normal tissue by the shear stiffness. The shear stiffness increase ratio taken from the Sinkus study was used for the lung simulations here, extrapolated to our frequency range of interest as described in the following text. For fibrosis and tumors, the shear stiffness was 1.5 and 3.33 times of those of the normal lung tissue, respectively. For lung fibrosis, the shear viscosity was taken so that the shear wave attenuation (governed by the imaginary part of the shear wave number) was the same as the normal lung. For the tumor, the increased shear viscosity always leads to smaller shear wave attenuation than the normal case; so the shear viscosity that leads to the largest shear wave attenuation was selected. In the case of fibrosis, the modified shear viscoelastic parameters were applied to the entire lung parenchyma, which also caused a slight change in compression wave speed. All other parameters in the FE simulation remained unchanged. Two spherical regions of diameter 30 and 20 mm were created in the FE lung model to represent local tumors, to which the modified shear viscoelastic parameters were applied. Table II lists the compression and shear wave speed for the lung fibrosis and tumor simulations at 500 and 800 Hz.

V. RESULTS AND DISCUSSION

The experimental and simulation results are shown in this section. The experiments and simulation results are always displayed in the same scale range. Simulations on these two cases with fewer elements (330 534 and 453 002 tetrahedral elements, respectively) gave nearly the same results as the presented simulations; so there was confidence that the models used here had more than sufficient resolution for the frequencies considered.

In Figs. 7 and 8, the lung normal surface velocity magnitude (dB m/s for 1 Pa input acoustic pressure) from the experiments and simulation are displayed for the same regions. The areas within the dashed line are the lung surfaces scanned in the experiment and the corresponding area in the simulation. In Fig. 7, the experiment and simulation show similar patterns of velocity amplitude distribution. The velocity amplitudes are largest in the central areas of the lung and then gradually decay in the peripheral areas. The lung surface response is asymmetric; generally, there is a larger area of high surface velocity on the left lung surface than on the right lung surface. The amplitude distribution from the experiment is slightly more mottled compared with the simulation. This may be due to noise in the measurement, which resulted in a smaller than actual value of velocity amplitude measured at some scanning points. In addition, the structural inhomogeneity inside the lung makes the sound transmission more complex than the current simulation can fully capture. The comparisons at 800 Hz also show similar patterns of velocity amplitude distributions between experiment and simulation, but simulation with airway network 1 is closer to experiment result than simulation with airway network 2.

In Figs. 7 and 8, it is seen that the lung periphery has lower velocity amplitudes from the simulation than from the measurement. One possible reason is that when sound propagates in the airway tree, each airway segment and alveolar sac expands and contracts and radiates acoustic energy into the lung parenchyma. As the very small airway segments and alveolar sacs were not modeled in the FE simulation, less energy couples into the lung parenchyma; so the lung surface motion from the simulation is smaller than that from the experiment.

Visual comparison of the two simulations with experiment in Figs. 7 and 8 suggests that the lung model with

TABLE II. Compression and shear wave speed (m/s) for normal lung, lung fibrosis and tumor.

	500 Hz	800 Hz
Normal		
c_p	$29.25 + 7.55i$	$31.81 + 9.12i$
c_s	$6.37 + 1.47i$	$6.82 + 1.68i$
Lung fibrosis		
c_p	$29.66 + 7.56i$	$32.18 + 9.11i$
c_s	$7.95 + 2.36i$	$8.53 + 2.69i$
Tumor		
c_p	$32.13 + 9.23i$	$34.47 + 10.40i$
c_s	$13.91 + 8.09i$	$14.78 + 8.54i$

TABLE I. Lung parenchyma and airway parameters in simulation.

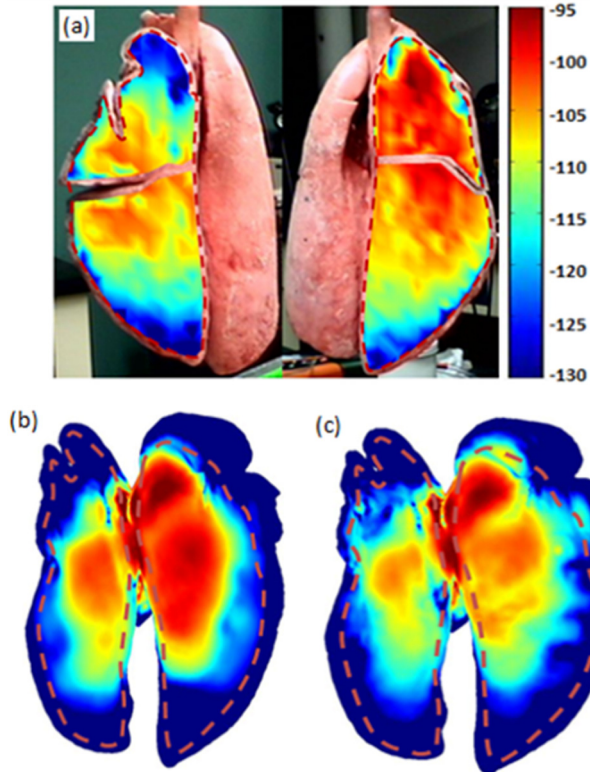|	500 Hz	800 Hz
c_p (m/s)	$29.25 + 7.55i$	$31.81 + 9.12i$
c_s (m/s)	$6.37 + 1.47i$	$6.82 + 1.68i$
E (MPa)	$0.28 + 1.55i$	$0.28 + 2.49i$
$Z_T^{(17)}$ (Pa s/m)	$18.76 + 51.10i$	$25.37 + 92.14i$
$Z_T^{(12)}$ (Pa s/m)	$10.76 + 16.09i$	$10.44 + 28.04i$

FIG. 7. (Color online) Lung normal surface velocity magnitude (dB m/s for 1 Pa input acoustic pressure) at 500 Hz (a) experiment; (b) simulation, lung with airway network 1; (c) simulation, lung with airway network 2.
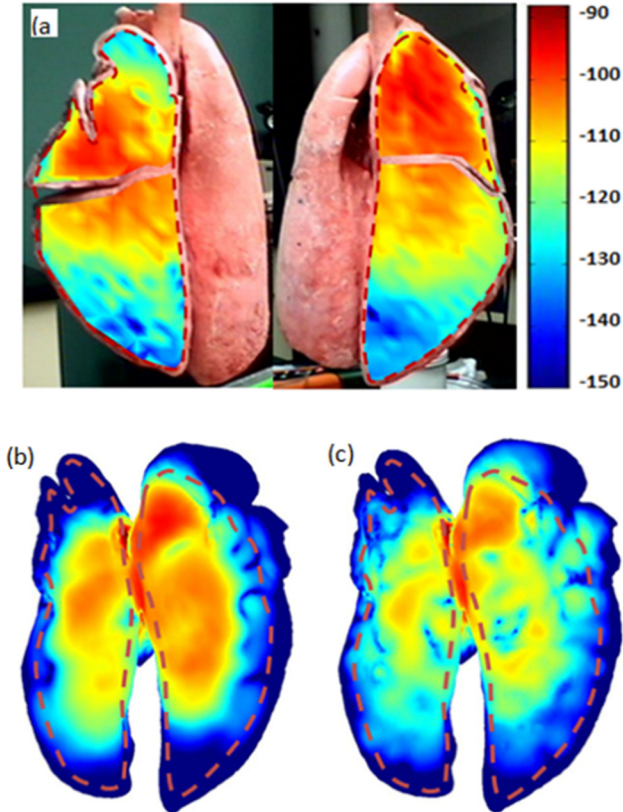

FIG. 8. (Color online) Lung normal surface velocity magnitude (dB m/s for 1 Pa input acoustic pressure) at 800 Hz (a) experiment; (b) simulation, lung with airway network 1; (c) simulation, lung with airway network 2.

airway network 1 provides a closer match to experiment than the model with airway network 2. This is also shown at most frequencies in the entire simulation frequency range. This seems counterintuitive as we might think that the more airway segments in the model, the closer the simulation to the experiment. The airway tree was constructed from CT images and the very small segments have relatively rough cylindrical shapes due to the CT resolution, which does not accurately represent the real case. This may contribute to airway network 1 results being closer to the experiment than airway network 2. Figure 9 shows the real part of airway acoustic pressure distribution at two different frequencies. For the large airway segments that both airway networks 1 and 2 have, their acoustic pressures are almost the same; this again shows that the simplified airway tree is nearly equivalent to the more detailed airway tree in terms of the airway acoustics of the larger airways. In Fig. 9 (b), the real part of the airway acoustic pressure at 800 Hz is negative in some locations as the phase shift at 800 Hz was greater than that at 500 Hz. It is also observed in Fig. 9 that sound pressure dramatically attenuates after several bifurcations; this suggests that most of the acoustic energy has left the airways and transmitted into the lung parenchyma prior to reaching the smaller segments represented in the airway network 2 model.

This suggests that the added complexity of network 2 is not necessary. Hence simulations of wave motion inside and on the surface of the lung will only be shown for airway network 1.

For computational model evaluation, four points on each side of the lung were selected, and the surface velocity
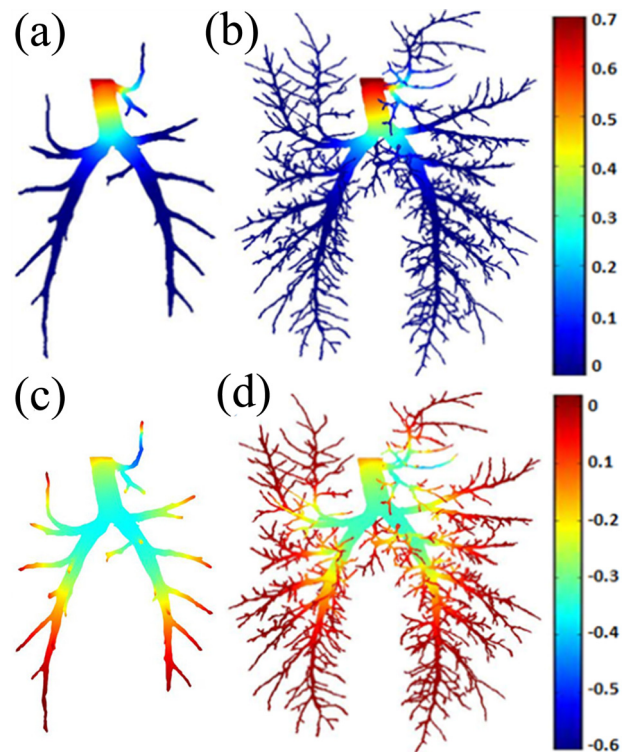

FIG. 9. (Color online) Real part of airway acoustic pressure (Pa): (a) 500 Hz, airway network 1; (b) 500 Hz, airway network 2; (c) 800 Hz, airway network 1; (d) 800 Hz, airway network 2.
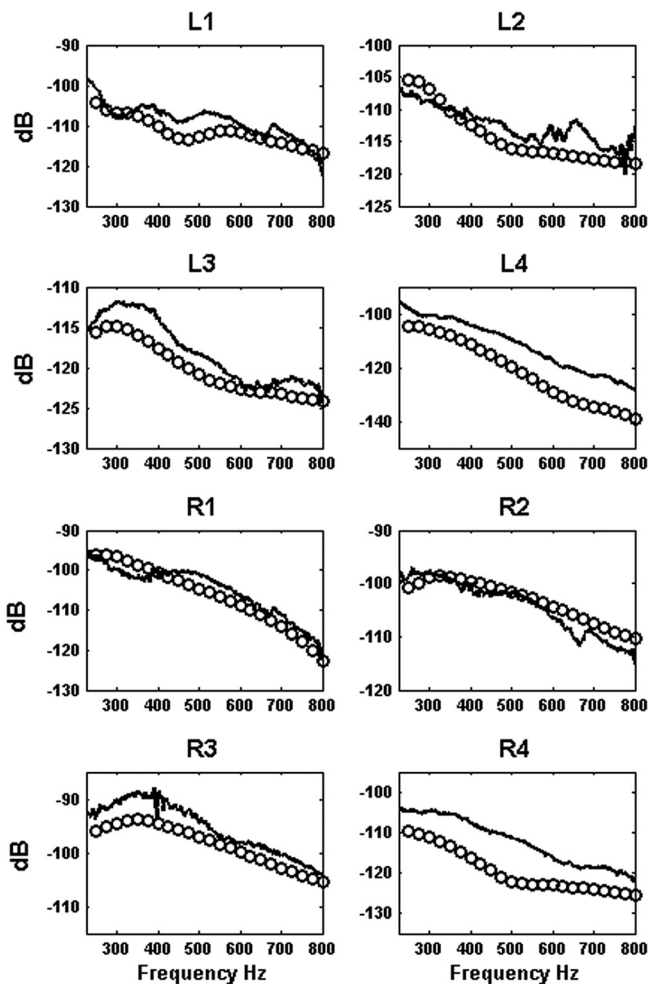
FIG. 10. Lung normal surface velocity magnitude (dB m/s for 1 Pa input acoustic pressure) at selected points [point locations are in Fig. 6(a)]. Key: —, experiment; ○○○, simulation.
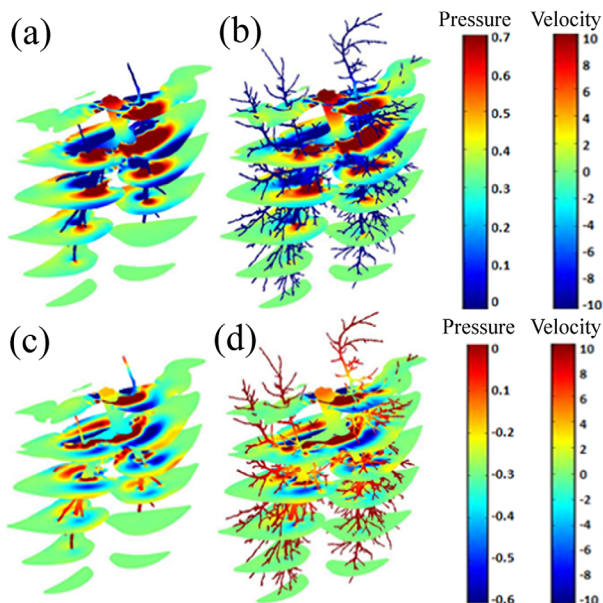

FIG. 11. (Color online) Stacked horizontal slices of the real part of the lung velocity (µm/s) in the anterior-posterior direction and airway acoustic pressure (Pa) (a) airway network 1 at 500 Hz; (b) airway network 2 at 500 Hz; (c) airway network 1 at 800 H; (d) airway network 2 at 800 Hz.
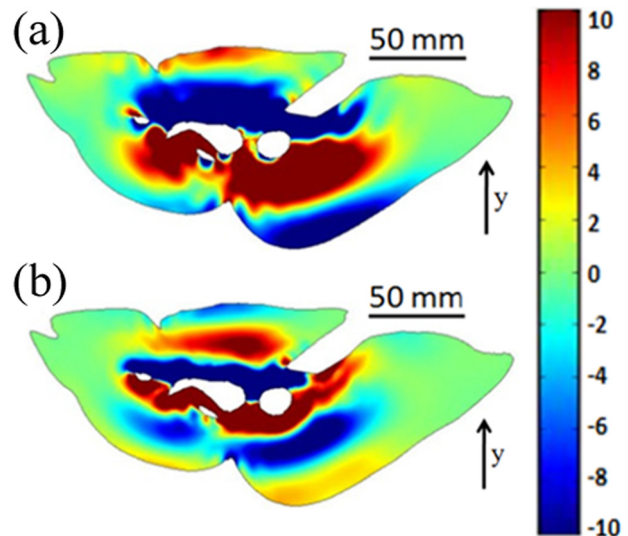

FIG. 12. (Color online) Cross-section images of the real part of the lung velocity (µm/s) in the anterior-posterior direction (see arrow) (a) 500 Hz, (b) 800 Hz.

amplitude at these points was compared with that measured on the preserved lung at the same locations. On each side of the lung, point 1 is in the top region, points 2 and 3 are in the central region while point 4 is in the bottom region. These points were selected to evaluate sound transmission in different parts of the lung by the computational model. Figure 10 shows the lung normal surface velocity magnitude with respect to 1 Pa input acoustic pressure. It is seen that the simulation (from lung model with airway network 1) captures the general trend in the experiment except that at point 4, the surface velocity predicted by simulation has some deviation in amplitude with experimental values. One cause of deviations at points 1–3 is that the terminal airway segment acoustic impedance was calculated based on the human lung Horsfield model. In the experiment, even though most of the sound energy couples into the lung parenchyma before reaching smaller segments, a small portion still transmits down through bronchioles and then reaches alveolar sacs. As it is computationally prohibitive to model millions of alveoli in the lung, the simplified airway model in the current study is another cause of the deviation in Fig. 10.

While the SLDV only measures the lung surface motion, the computer simulations enable exploration of sound transmission inside the lung. Wave motion inside the lung can also be seen from the simulation. In Fig. 11, five stacked horizontal slices spaced at 50 mm display the real part of the lung velocity (µm/s) in the anterior-posterior direction together with airway acoustic pressure (Pa). Cross-section images of the second top horizontal slice are shown in Fig. 12. The real part of the velocity is in the y direction

TABLE III. Compression wave length (mm) estimation from simulation compared to Biot theory.

	500 Hz	800 Hz
Biot theory	61.3	42.8
Simulation	60	38

Dai *et al.*: Computational lung sound transmission model
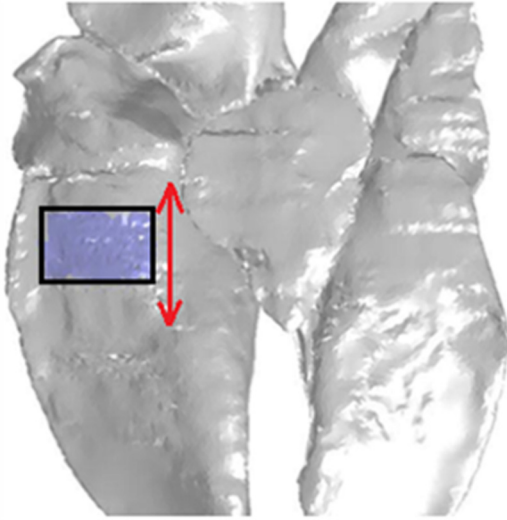
FIG. 13. (Color online) Shear motion applied to the lung surface.

FIG. 15. (Color online) Cross-section images of the real part of the lung velocity (mm/s) in the anterior-posterior direction (see arrow) at 800 Hz: (a) normal lung, (b) fibrotic lung.

(anterior-posterior direction). Wave propagations are seen more clearly in the cross-section images. These are compression waves based on the wave length. The shear wave length is smaller than the compression wave length, and from Fig. 12 it is seen that the compression wave is dominant in the lung caused by airway insonification; this is also reported in previous studies.[25,26] Table III lists the wavelength estimated at 500 and 800 Hz and comparison with Biot theory predictions. It is found that at 500 and 800 Hz, the wavelength estimated from simulation generally agrees well with Biot theory predictions even though reflections of finite boundaries in the simulation cause small deviations.

Diffuse lung fibrosis causes much smaller changes in compression wave speed in the lung compared to changes in shear wave speed as calculated from Biot theory of poroviscoelasticity and seen from Table II. So the very small differences in compression wave length in cross-section images of the real part of the lung velocity are too weak to show alterations of wave propagation caused by diffuse fibrosis.

Changes in shear wave length could be a better way to separate fibrotic lung from the normal lung.

So shear waves were induced in the simulation by applying a harmonic shear force to the lung surface of 1 mm amplitude over an area of about 6.5×4 cm as shown in Fig. 13. Cross-section images of shear waves are shown in Figs. 14 and 15. As wave images are mainly used to highlight the wavelength changes caused by diffuse fibrosis and the airway details do not greatly affect the wave fields, only simulations on airway network 1 are presented here. For both frequencies, the shear wavelength for lung fibrosis increases [as seen in Fig. 14(b) and Fig. 15(b)] due to the increased shear stiffness. Table IV lists the shear wavelength estimated from simulation, which can differentiate the normal from the fibrotic lung.

Figure 16 shows the cross-section images of the real part of the velocity (μm/s) at 500 and 800 Hz for the lung with local tumor. Compared with Fig. 12, the compression wave length at each frequency remains almost the same while the wave fields are distorted by the tumors. Due to the impedance mismatch between the tumors and surrounding lung parenchyma, part of the tumor boundary where it is close to the main stem-bronchi is clearly visible.

In terms of the simulation of sound transmission in the lung via input from trachea, the current model is more comprehensive than other models reported in the literature to the best knowledge of the authors. It is acknowledged that the excised preserved lung will have differences from the *in vivo* case that may have an effect on its acoustic characteristics.
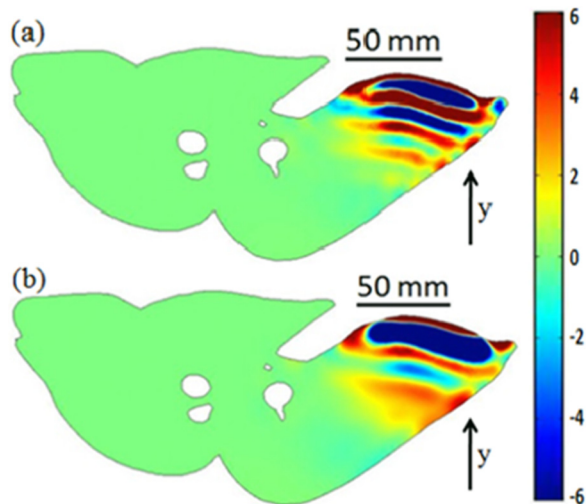

FIG. 14. (Color online) Cross-section images of the real part of the lung velocity (mm/s) in the anterior-posterior direction (see arrow) at 500 Hz: (a) normal lung, (b) fibrotic lung.
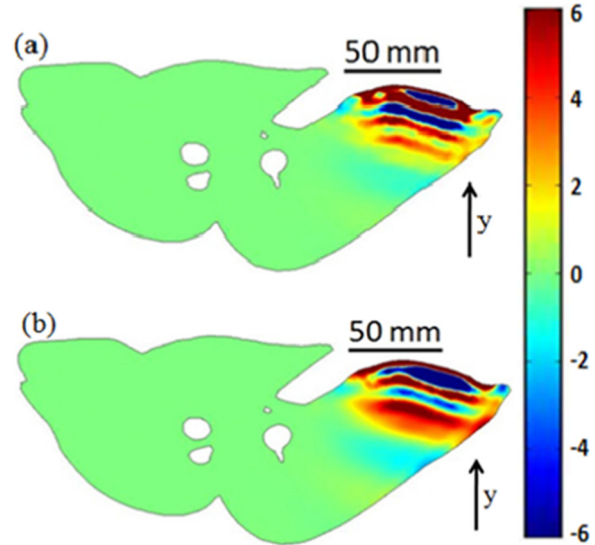
TABLE IV. Normal and fibrotic lung shear wavelength (mm) from simulation.

	500 Hz	800 Hz
Normal	14.01	10.39
Fibrotic	17.88	12.69

J. Acoust. Soc. Am., Vol. 136, No. 3, September 2014

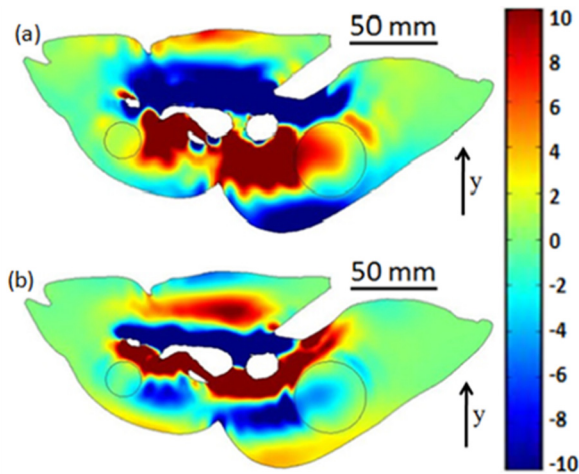Dai *et al.*: Computational lung sound transmission model   1427

FIG. 16. (Color online) Cross-section images the real part of the velocity (μm/s) in the anterior-posterior direction for the lung with tumor: (a) 500 Hz, (b) 800 Hz.

Based on studies of others and of ours *in vivo* or *in situ* immediately upon sacrifice, we do not believe these effects are large at least at the acoustic macroscopic scale.

VI. CONCLUSIONS

A comprehensive computational simulation model of sound transmission through a porcine excised lung is presented and experimentally evaluated. Parenchymal and major airway geometry of this "subject-specific" model was created from x ray CT images. The vibroacoustic response of the lung to sound input at the trachea is simulated in COMSOL FE software. The lung parenchyma is modeled as a poroviscoelastic material using Biot theory. Acoustic impedances were applied at the airway terminal segments to represent the downstream unmodeled airway segments. The FE simulations were validated by comparisons with experimental measurements obtained using scanning laser Doppler vibrometry on the surface of an excised, preserved lung. Two levels of airway detail were used in the FE simulations, and the model with fewer airway segments was closer to experimental measurements. The FE model was also used to visualize vibroacoustic pressure and motion inside the lung and its airways caused by the acoustic input. Effects of diffuse lung fibrosis and localized tumors on the lung acoustic response were visualized from FE simulations. This type of visualization could potentially be compared and matched with images from elastography measurements to better quantify lung material properties, such as stiffness.

ACKNOWLEDGMENTS

[1]Q. Chen, V. M. Mai, A. A. Bankier, V. J. Napadow, R. J. Gilbert, and R. R. Edelman, "Ultrafast MR grid-tagging sequence for assessment of local mechanical properties of the lungs," Magn. Reson. Med. **45**(1), 24–28 (2001).

[2]V. J. Napadow, V. M. Mai, A. A. Bankier, R. J. Gilbert, R. R. Edelman, and Q. Chen, "Determination of regional pulmonary parenchymal strain during normal respiration using spin inversion tagged magnetization," J. Magn. Reson. Imaging **13**(3), 467–474 (2001).

[3]H. A. Mansy, R. Balk, T. J. Royston, and R. H. Sandler, "Pneumothorax detection using pulmonary acoustic transmission measurements," Med. Biol. Eng. Comput. **40**, 520–525 (2002).

[4]H. A. Mansy, R. Balk, T. J. Royston, and R. H. Sandler, "Pneumothorax detection using computerized analysis of breath sounds," Med. Biol. Eng. Comput. **40**, 526–532 (2002).

[5]H. Pasterkamp, R. Consunji-Araneta, Y. Oh, and J. Holbrow, "Chest surface mapping of lung sounds during methacholine challenge," Pediatr. Pulmonol. **23**, 21–30 (1997).

[6]M. Kompis, H. Pasterkamp, and G. R. Wodicka, "Acoustic imaging of the human chest," Chest **120**, 1309–1321 (2001).

[7]G. Benedetto, F. Dalmasso, and R. Spagnolo, "Surface distribution of crackling sounds," IEEE Trans. Biomed. Eng. **35**, 406–412 (1988).

[8]S. Charleston-Villalobos, S. Cortes-Rubiano, R. Gonzalez-Camarena, G. Chi-Lem, and T. Aljama-Corrales, "Respiratory acoustic thoracic imaging (RATHI): Assessing deterministic interpolation techniques," Med. Biol. Eng. Comput. **42**, 618–626 (2004).

[9]T. Bergstresser, D. Ofengeim, A. Vyshedskiy, J. Shane, and R. Murphy, "Sound transmission in the lung as a function of lung volume," J. Appl. Physiol. **93**, 667–674 (2002).

[10]R. Paciej, A. Vyshedskiy, J. Shane, and R. Murphy, "Transpulmonary speed of sound input into the supraclavicular space," J. Appl. Physiol. **94**, 604–611 (2003).

[11]Y. Peng, Z. Dai, H. A. Mansy, R. H. Sandler, and T. J. Royston, "Sound transmission in the chest under surface excitation: an experimental and computational study with diagnostic applications," Med. Biol. Eng. Comput. (2013).

[12]B. C. Goss, K. P. McGee, E. C. Ehman, A. Manduca, and R. L. Ehman, "Magnetic resonance elastography of the lung: technical feasibility," Magn. Reson. Med. **56**, 1060–1066 (2006).

[13]K. P. McGee, R. D. Hubmayr, and R. L. Ehman, "MR elastography of the lung with hyperpolarized ³He," Magn. Reson. Med. **59**, 14–18 (2008).

[14]K. P. McGee, D. Lake, Y. K. Mariappan, R. D. Hubmayr, A. Manduca, K. Ansell, and R. L. Ehman, "Calculation of shear stiffness in noise dominated magnetic resonance elastography data based on principal frequency estimation," Phys. Med. Biol. **56**, 4291–4309 (2011).

[15]Y. K. Mariappan, A. Kolipaka, A. Manduca, R. D. Hubmayr, R. L. Ehman, P. Araoz, and K. P. McGee, "Magnetic resonance elastography of the lung parenchyma in an in situ porcine model with a noninvasive mechanical driver: Correlation of shear stiffness with trans-respiratory system pressures," Magn. Reson. Med. **67**, 210–217 (2012).

[16]R. Sinkus, M. Tanter, T. Xydeas, S. Catheline, J. Bercoff, and M. Fink, "Viscoelastic shear properties of in vivo breast lesions measured by MR elastography," Magn. Reson. Imaging **23**(2), 159–165 (2005).

[17]N. S. Shah, S. A. Kruse, D. J. Lager, G. Farell-Baril, J. C. Lieske, B. F. King, and R. L. Ehman, "Evaluation of renal parenchymal disease in a rat model with magnetic resonance elastography," Magn. Reson. Med. **52**(1), 56–64 (2004).

[18]J. Kemper, R. Sinkus, J. Lorenzen, C. Nolte-Ernsting, A. Stork, and G. Adam, "MR elastography of the prostate: initial in-vivo application," Rofo **176**(8), 1094–1099 (2004).

[19]T. R. Jenkyn, R. L. Ehman, and K. An, "Noninvasive muscle tension measurement using the novel technique of magnetic resonance elastography (MRE)," J. Biomech. **36**(12), 1917–1921 (2003).

[20]D. Klatt, U. Hamhaber, P. Asbach, J. Braun, and I. Sack, "Noninvasive assessment of the rheological behavior of human organs using multifrequency MR elastography: A study of brain and liver viscoelasticity," Phys. Med. Biol. **52**(24), 7281–7294 (2007).

[21]K. Horsfield and G. Cumming, "Morphology of the bronchial tree in man," J. Appl. Physiol. **24**, 373–383 (1968).

[22]K. Horsfield, W. Kemp, and S. Phillips, "An asymmetrical model of the airways of the dog lung," J. Appl. Physiol. **52**, 21–26 (1982).

[23]J. J. Fredberg and J. A. Moore, "Distributed response of complex branching duct networks," J. Acoust. Soc. Am. **63**, 954–961(1978).

[24]D. A. Rice, "Sound speed in pulmonary parenchyma," J. Appl. Physiol. **54**, 304–308 (1983).

[25]G. R. Wodicka, K. N. Stevens, H. L. Golub, E. G. Cravalho, and D. C. Shannon, "A model of acoustic transmission in the respiratory system," IEEE Trans. Biomed. Eng. **36**, 925–934 (1989).

[26]T. J. Royston, X. Zhang, H. A. Mansy, and R. H. Sandler, "Modeling sound transmission through the pulmonary system and chest with application to diagnosis of a collapsed lung," J. Acous. Soc. Am. **111**(4), 1931–1946 (2002).

[27]M. Siklosi, O. E. Jensen, R. H. Tew, and A. Logg, "Multiscale modeling of the acoustic properties of lung parenchyma," ESAIM Proc. **23**, 78–97 (2008).

Dai *et al.*: Computational lung sound transmission model

[28] Z. Dai, Y. Peng, T. J. Royston, H. A. Mansy, and R. H. Sandler, "Comparison of poroviscoelastic models for sound and vibration in the lungs," J. Vib. Acous. (2014).

[29] R. H. Habib, R. B. Chalker, B. Suki, and A. C. Jackson, "Airway geometry and wall mechanical properties estimated from subglottal input impedance in humans," J. Appl. Physiol. **77**, 441–451 (1994).

[30] R. H. Habib, B. Suki, J. H. Bates, and A. C. Jackson, "Serial distribution of airway mechanical properties in dogs: Effects of histamine," J. Appl. Physiol. **77**, 554–566 (1994).

[31] T. J. Royston, M. B. Ozer, S. Acikgoz, H. A. Mansy, and Sandler R. H., "Advances in computational modeling of sound propagation in the lungs and torso with diagnostic applications," in *Vibration and Acoustics in Biomedical Applications: Imaging, Characterization and Diagnostics* (ASME Press, New York, 2008), pp. 215–246.

[32] A. B. Dubois, A. W. Brody, D. H. Lewis, and B. F. Burgess, Jr., "Oscillation mechanics of lungs and chest in man," J. Appl. Physiol. **8**, 587–594 (1956).

[33] M. Schanz, *Wave Propagation in Viscoelastic and Poroelastic Continua: A Boundary Element Approach* (Springer, Berlin, 2001), pp. 77–82.

[34] B. Suki, R. H. Habib, and A. C. Jackson, "Wave propagation, input impedance, and wall mechanics of the calf trachea from 16 to 1,600 Hz," J. Appl. Physiol. **75**(6), 2755–2766 (1993).

[35] T. J. Royston, Z. Dai, R. Chaunsali, Y. Liu, Y. Peng, and R. L. Magin, "Estimating material viscoelastic properties based on surface wave measurements: A comparison of techniques and modeling assumptions," J. Acous. Soc. Am. **130**(6), 4126–4138 (2011).

[36] T. Ebihara, N. Venkatesan, R. Tanaka, and M. S. Ludwig, "Changes in extracellular matrix and tissue viscoelasticity in bleomycin-induced lung fibrosis: Temporal aspects," Am. J. Respir. Crit. Care Med. **162**(4), 1569–1576 (2000).

[37] F. Liu, J. D. Mih, B. S. Shea, A. T. Kho, A. S. Sharif, A. M. Tager, and D. J. Tschumperlin, "Feedback amplification of fibrosis through matrix stiffening and COX-2 suppression," J. Cell. Biol **190**(4), 693–706 (2010).